Geomechanics and Engineering, *Vol. 19, No. 5 (2019) 421-434*
DOI: https://doi.org/10.12989/gae.2019.19.5.421

Numerical study on mechanical and failure properties of sandstone based on the power-law distribution of pre-crack length

Hao Shi[1,2], Lei Song*[1], Houquan Zhang[1], Keke Xue[1], Guotao Yuan[1], Zhenshuo Wang[1] and Guozhu Wang[1]

[1]*State Key Laboratory for Geomechanics & Deep Underground Engineering, School of Mechanics & Civil Engineering, China University of Mining and Technology, Xuzhou, 221008, People's Republic of China*
[2]*University of Nottingham, GeoEnergy Research Centre, Nottingham NG7 2RD, U.K.*

(Received July 7, 2019, Revised November 25, 2019, Accepted November 27, 2019)

Abstract. It is of great significance to study the mechanical properties and failure mechanism of the defected rock for geological engineering. The defected sandstone modeling with power-law distribution of pre-cracks was built in this paper by Particle Flow Code software. Then the mechanical properties of sandstone and the corresponding failure process were meticulously analyzed by changing the power-law index (PLI) and the number of pre-cracks (NPC). The results show that (1) With the increase of the PLI, the proportion of prefabricated long cracks gradually decreases. (2) When the NPC is the same, the uniaxial compressive strength (UCS) of sandstone increases with the PLI; while when the PLI is the same, the UCS decreases with the NPC. (3) The damage model of rock strength is established based on the Mori-Tanaka method, which can be used to better describe the strength evolution of damaged rock. (4) The failure mode of the specimen is closely related to the total length of the pre-crack. As the total length of the pre-crack increases, the failure intensity of the specimen gradually becomes weaker. In addition, for the specimens with the total pre-crack length between 0.2-0.55 m, significant lateral expansion occurred during their failure process. (5) For the specimens with smaller PLI in the pre-peak loading process, the concentration of the force field inside is more serious than that of the specimens with larger PLI.

Keywords: numerical statistical study; mechanical property; failure mechanism; power-law distribution; defected sandstone

1. Introduction

As the natural material affected by temperature, chemical erosion and tectonic movement, the rock mass contains certain defects (like joints and cracks) ranging in size from sub-micron to kilometers (Al-Aasm *et al.* 2019, Lenton *et al.* 2015). Taking the Hornelen Basin in western Norway as an example, the defects in the rock mass have been greatly developed due to long-term effects of freeze-thaw cycle and ocean erosion (Lei and Gao 2019; Wang *et al.* 2019), as shown in Fig. 1. In addition, randomly distributed defects lead to heterogeneity and anisotropy of the nature material, which in turn results in its very complex mechanical properties and failure mechanisms. Unclear understanding of which makes it difficult to effectively prevent and control rock disasters (Zhu and Yang 2018), which will bring huge security risks to the construction of rock salt storage, nuclear waste storage, and coal mining (Basson and Viola 2003, Shan and Lei 2019, Wang and Tian 2018). Therefore, it is of great significance to study the mechanical properties and failure mechanism of fractured rock mass in depth.

At present, the study on the defected rock mass is a hot topic in rock mechanics research (Huang *et al.* 2016, Lei and Gao 2019, Wang and Tian 2018). Among which, the current research can be roughly divided into two categories according to the number of pre-cracks (NPCs) contained in the specimen.

For the first type, the NPC is generally less than 4, and the specimen is mainly made by hydraulic cutting (experiment) or discrete particle deletion (simulation). Yang *et al.* (2014, 2016), had conducted a large number of studies in this aspect, mainly prefabricated multiple fissures to study the effect of their combination on rock mechanical properties. What's more, Wang and Tian (2018) studied the failure mechanism of coal-rock under different combinations of prefabricated cracks and holes. Afolagboye *et al.* (2017) as well as Zhang and Zhang (2017) conducted detailed studies on the crack propagation process at the rock bridge. The above studies are of great significance for understanding the mechanical properties of rock masses with prefabricated defects. However, the small number, subjective angle and size distribution of the defects lead to the research results without a high universal significance. In addition, due to the limitations of hydraulic cutting and particle deletion, the defect in the above study cannot be called a crack for its too large width, for example, the crack width of 2 mm is used in the research of Wang and tian (2018).

For the second type, the NPC contained inside the specimen reaches hundreds of thousands, which is made mainly by probability distribution or the combined of the stratigraphic scanning and computer extraction. Lei and

*Corresponding author, Professor
E-mail: songlei_cumt@163.com

ISSN: 2005-307X (Print), 2092-6219 (Online)

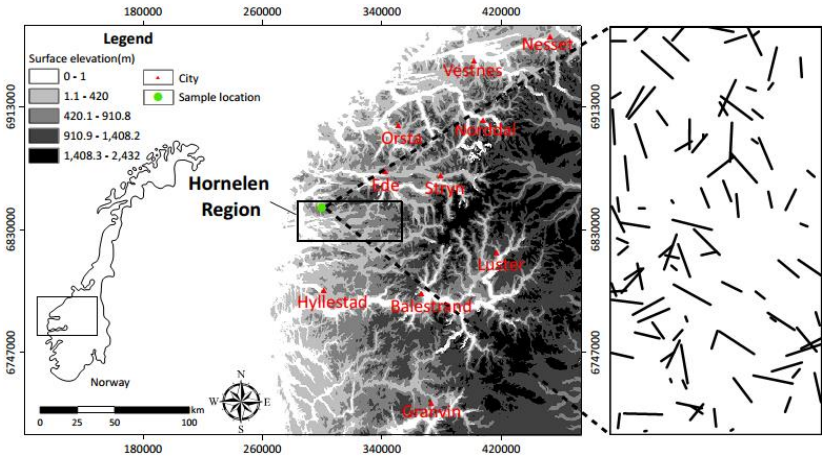

Fig. 1 Outcrop map of the natural fracture system in the sandstone at Hornelen Basin, western Norway (Lei and Gao 2019)

Gao (2019), as well as Odling (1997) numerically studied the heterogeneity of rock materials based on pre-crack Weibull distribution. Chen *et al.* (2018) studied the influence of the average length and NPC on the acoustic wave field of rock based on the power-law distribution (PLD) of the crack length. Wang *et al.* (2018) and Yang *et al.* (2018) studied the effects of joint parameters (such as joint geometry roughness) on the shear properties and uniaxial compressive strength (UCS) of fractured rock masses respectively. The second type of research enriches the study of rock masses with a large number of defects. However, the influences of pre-crack distribution on rock strength and new crack propagation are not taken into consideration.

Therefore, the FISH language of Particle Flow Code in two dimensions (PFC2D) is used in this paper to generate the defected specimens with pre-crack length following PLD. Then the power-law index (PLI) and the NPC are changed to statistically study their effects on the mechanical properties of sandstone and meticulously analyze the corresponding failure process. At the same time, the damage model with pre-crack length following PLD is also established in this paper.

2. Equation of PLD for crack length

The PLD equation can be described as follows,

$$y = ax^{-\frac{1}{b-1}} \tag{1}$$

where a (>0) and b (>1) are unknown coefficients, among which, b, as the PLI, is one of the two main variables studied in this paper.

To determine the specific PLD, the maximum length l_{max}, minimum length l_{min} and PLI b of the pre-cracks need to be given in advance. According to the increase-decrease characteristics of Eq. (1), the following relationships can be established,

$$\begin{cases} ax_{\max}^{-\frac{1}{b-1}} = l_{\min} \\ ax_{\min}^{-\frac{1}{b-1}} = l_{\max} \end{cases} \tag{2}$$

where x_{min}, x_{max} are the lower bound and upper bound of independent variables for PLD of crack length, from which the range of the independent variable x can be determined as $x_{min}<x<x_{max}$.

However, Eq. (2), as a hyperstatic equation, contains three unknowns a, x_{max} and x_{min}, so the value of one of the parameters must be assigned (which does not affect the results), for convenience, the following formula can be assumed,

$$a=1 \text{ or } x_{max}=1 \text{ or } x_{min}=1 \tag{3}$$

The PLD of the crack length can be obtained by Eqs. (2)-(3). In addition, the corresponding crack length can be acquired by linear interpolation (theoretical) and probability assignment (simulation) with the given pre-crack number n_p.

3. PFC numerical model based on PLD of pre-crack length

3.1 Particle bonding model

The PFC2D software, with excellent simulation effects on rock mechanics and crack propagation process, characterizes geotechnical media by particles and bonds. The particle, represented by the disk with unit thickness (in PFC2D), is the rigid body with normal and tangential stiffness; For the bonding model between particles, there are two main types suitable for rock simulation, namely contact and parallel bonds, as shown in the Fig. 2. The contact bond can only reflect the normal and tangential action (force) between particles; while the parallel bond can transmit both the force and moment. Obviously, the two bonds, both should be included inside the rock, are used in this article.

3.2 Calibration of mesoscopic parameters for intact sandstone

Numerical simulation needs to determine the model parameters after the establishment of the numerical model. As described in Section 3.1 that the basic elements of the

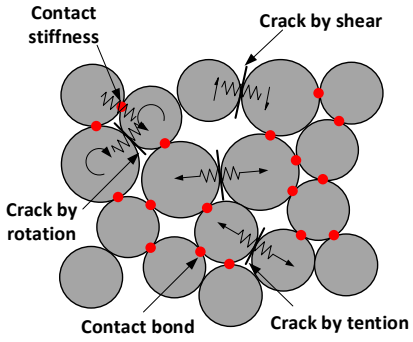

(a) Contact bond model

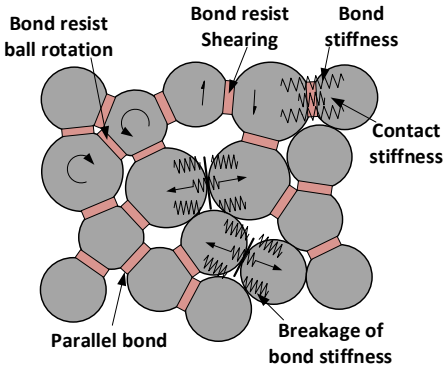

(b) Parallel bond model

Fig. 2 Cohesive model and its micro-mechanical behavior schematic diagram (Storey *et al.* 2013, Wang and tian 2018)

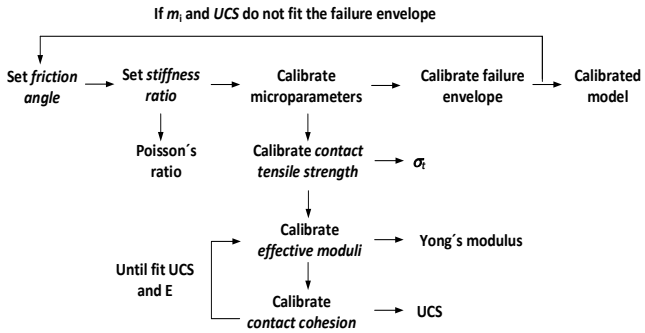

Fig. 3 The "trial and error" method parameter checking process of PFC model (Castro-Filgueira *et al.* 2017)

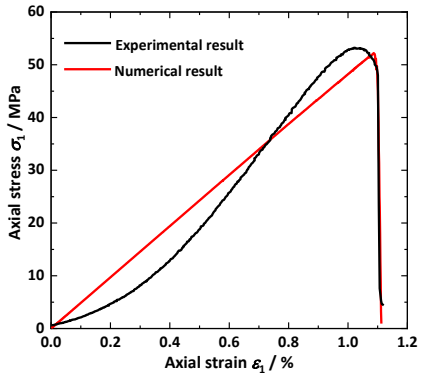

Fig. 4 The comparison between the numerical and experimental stress–strain curves of intact sandstone specimen

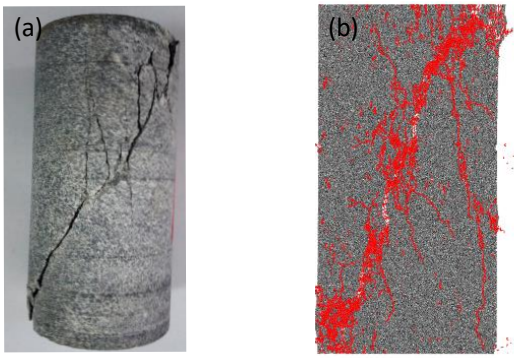

(a) Experimental failure mode (b) Numerical failure mode

Fig. 5 Failure modes of intact sandstone specimens obtained through simulation and experiment

Table 1 Mesoscopic parameters of PFC^{2D} medium

Parameters	Value	Parameters	Value
Minimum particle size (mm)	0.1	Friction coefficient	0.8
Maximum particle size (mm)	0.3	Parallel bond tensile strength (MPa)	26.5
Density (kg•m^{-3})	2700	Parallel bond cohesion (MPa)	32
Porosity	0.15	Parallel bond friction angle (°)	32.5
Contact bond modulus (GPa)	0.6	Parallel bond modulus (GPa)	8.7
Contact bond stiffness ratio	1.0	Parallel bond stiffness ratio	1.0

Table 2 Mechanical parameters of smooth joint model

Parameters	Value
Normal stiffness per unit area (GPa)	2
Shear stiffness per unit area (GPa)	2
Friction coefficient	0.35
Tensile strength (Pa)	0
Cohesion (Pa)	0

PFC model are the particles and the bond between the particles, so the mesoscopic parameters, need to be inputted to reflect their physical and mechanical properties, cannot be directly obtained from the laboratory. The researchers usually select the full stress-strain curve and the corresponding failure mode obtained from laboratory rock compression test as a reference, and use the "trial and error" method (the method for Unconfined Compressive Strength (UCS) test is shown in Fig. 3, where m_i is the strength parameter of Hoek-Brown) to adjust the mesoscopic parameters until that the simulation curve and failure mode are basically consistent with that of the experiment. Then the determined parameters are considered to be able to reflect the mechanical properties of the rock and can be used as the basis parameters for further research (Castro-Filgueira *et al.* 2017).

In this paper, the UCS test of standard sandstone specimen was carried out to obtain the referenced stress-strain curve and failure mode by the 815 test machine of the Deep Geotechnical and Underground Engineering

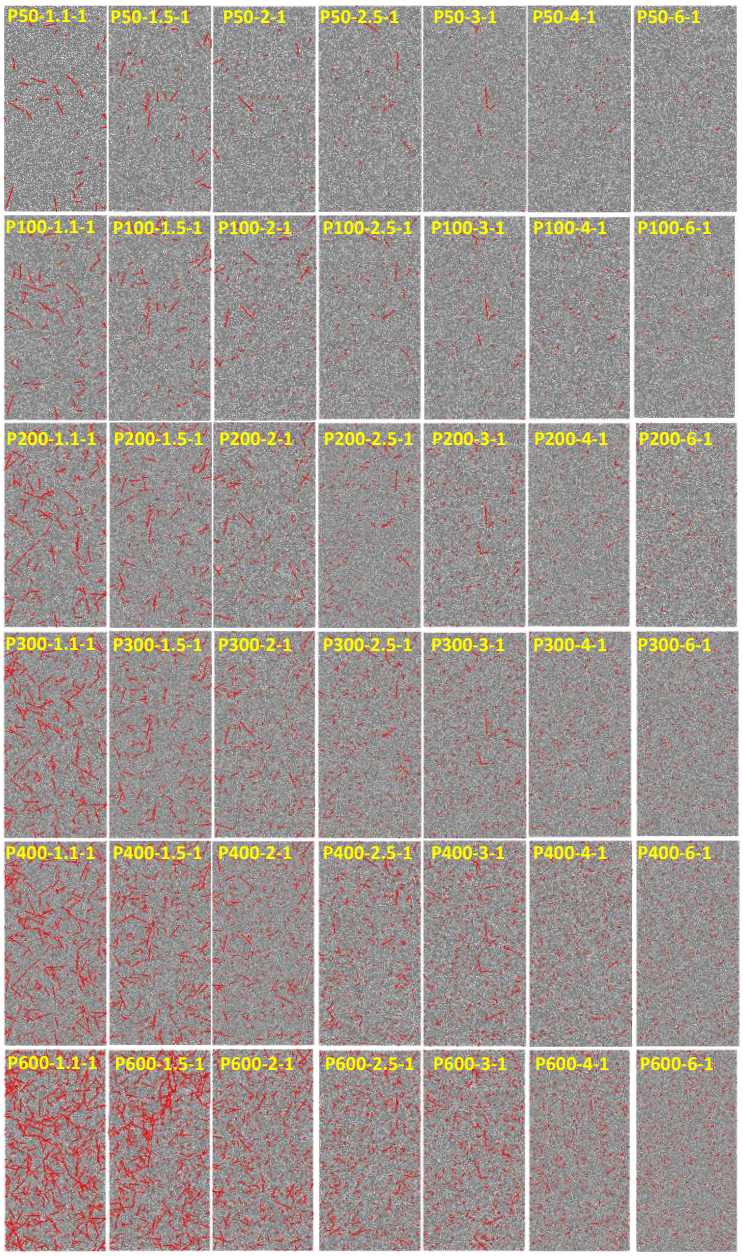

Fig. 6 Selected samples of sandstone specimen with different NPCs

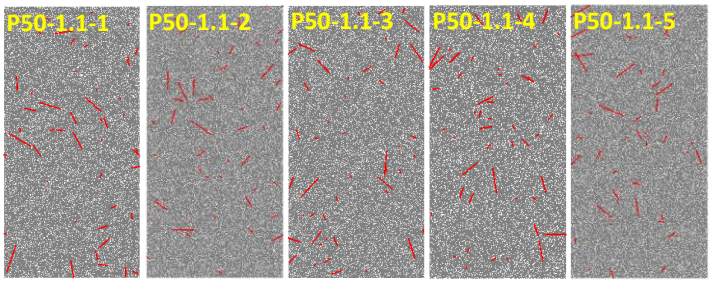

Fig. 7 Sandstone specimen models with pre-crack number of 50 and the PLI of 1.1

Laboratory, China University of Mining and Technology. Then the numerical model with 31190 particles and the size of 50×100 mm was established using PFC2D. Finally, setting the same loading rate (0.002 mm/s) as that of the laboratory specimen and determined the mesoscopic parameters of the numerical model using the "trial and error" method. It should be pointed out that although the experimental specimens have been screened for texture and appearance, a certain amount of natural cracks or defects are inevitably contained inside the sample. In view of the

fact that the prefabricated crack density and scale of the numerical model in this article are relatively large, the laboratory sandstone can be seen as non-destructive specimen to calibrate the mesoscopic parameters.

The comparison between simulation and experimental results is shown in Figs. 4 and 5. According to the figures, the full stress-strain curve and failure mode obtained by experiment and simulation are basically the same (the relative errors of peak strength and peak strain are 1.7% and 3.8%, respectively, see Fig. 4), but the simulated curve and the experimental curve are slightly different in the pre-peak stage. Considering that the compaction stage of rock cannot be simulated by the current numerical simulation software and the strength characteristic of rock rather than the elastic modulus is the studied object, the calibrated parameters in table 1 can be considered suitable.

The sandstone mesoscopic parameters obtained by calibration are shown in Table 1.

3.3 Establishment of numerical model with pre-crack

In PFC2D software, a fracture, as the planar, finite-size and discrete element, is modeled by a segment, the two extremities of the segment are vertex objects used to realize the prefabricating of the fracture by Discrete Fracture Network (DFN) module. The general prefabricating steps are as follows, (1) setting the DFN template involved the orientation range, the length range as well as their respective distribution modes (including the position); (2) generating the cracks by setting the pre-cracks number (n_p) and their distribution range; (3) assigning the attribute parameters of DFN model.

In this paper, the ranges of crack size and angle are 0.5-10 mm and 0-180°, respectively. What's more, the crack angle and position are set to be randomly distributed to reduce the number of variables, but the crack size follows the PLD as mentioned above. The numerical models generated in this paper are divided into 6 big groups according to pre-crack numbers of 50/ 100/ 200/ 300/ 400/ 600, and each big group is divided into 7 small groups according to the difference of PLI (the PLIes of each small group are 1.1/ 1.5/ 2/ 2.5/ 3/ 4and 6 respectively). Which is to say that there are 42 small groups. And in order to reduce the influence of random pre-crack distribution on the dispersion of rock strength, 5 specimens are generated in each small group. Therefore, a total number of 210 specimens were established in this paper, which could be considered sufficient for the purpose of statistical research on the relationship between rock pre-crack and strength.

In addition, the PLD range is the same as the specimen range; the smooth joint model and the default model parameters (see Table 2) are used to describe the mechanical properties of the pre-cracks (Castro-Filgueira *et al.* 2017). It can be seen from Table 2 that main effect of the pre-cracks is to destroy the cohesion effect between the media on both sides of the crack face.

One sample in each small group is selected to display as shown in Fig. 6. The combination of letter and number in the upper right corner of the specimens denotes the specimen number, where the letter P stands for "pre-crack", the remaining three numbers represent the NPC, the PLI of the pre-crack length and called times of the DFN module, respectively.

Taking the small group 1 (n_p=50, b=1.1) as an example, the 5 numerical models in the small group are shown in Fig. 7.

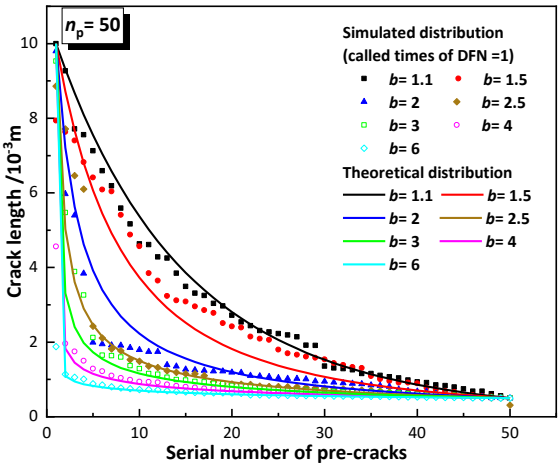

Fig. 8 Theoretical and actual simulated distribution for crack lengths with different PLIes

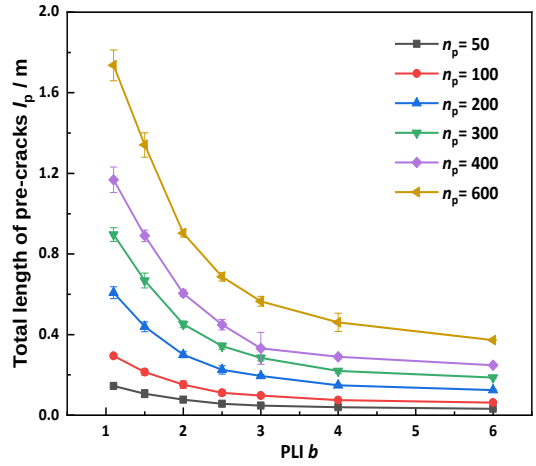

(a) Variation of total length with the PLI

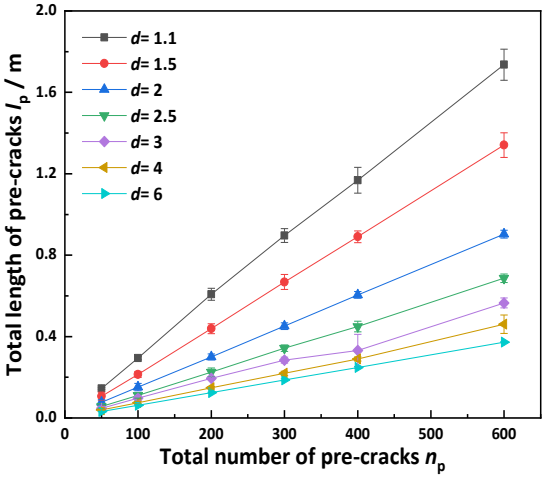

(b) Variation of total length with the NPC

Fig. 9 Relationship between the total length, the PLI and the NPC of pre-cracks

Table 3 UCS and crack information of each specimen

Pre-crack		UCS (MPa)						Total length of pre-cracks (10^{-2} m)					
		Called times of DFN model					Mean	Called times of DFN model					Mean
NPC	PLI	1	2	3	4	5		1	2	3	4	5	
50	1.1	21.96	26.57	**26.53***	25.42	29.43	25.98	14.54	14.12	14.46	14.11	15.20	14.49
	1.5	38.76	28.39	27.54	38.04	**29.21***	32.39	12.96	9.69	12.39	8.15	10.19	10.68
	2	34.15	29.89	31.86	**37.14***	45.53	35.71	7.43	9.03	8.70	7.36	5.86	7.68
	2.5	39.40	43.41	42.47	**44.35***	51.61	44.25	7.18	5.66	6.78	4.45	4.13	5.64
	3	**49.35***	46.38	48.52	49.50	51.95	49.14	6.11	4.84	4.36	4.71	3.83	4.77
	4	50.24	47.13	50.29	45.85	**47.76***	48.25	4.19	4.19	3.49	3.96	3.77	3.92
	6	52.51	**51.86***	52.45	51.61	51.79	52.04	3.29	3.31	3.02	3.20	3.14	3.19
100	1.1	14.59	**17.08***	17.15	14.65	18.09	16.31	28.66	28.57	29.52	30.16	30.36	29.45
	1.5	19.85	**23.30***	24.30	23.49	23.44	22.88	22.65	20.54	19.17	22.36	22.02	21.35
	2	21.43	26.31	40.78	**28.35***	38.88	31.15	16.46	16.06	12.52	16.79	14.02	15.17
	2.5	36.71	37.22	46.48	38.17	**38.64***	39.45	12.84	11.23	9.18	11.28	10.84	11.07
	3	42.48	42.14	**42.12***	32.77	49.36	41.78	10.95	9.07	8.71	10.66	9.35	9.75
	4	**47.50***	45.48	47.21	49.68	51.01	48.17	8.37	7.45	7.88	6.87	6.99	7.51
	6	46.25	51.81	52.06	**51.68***	53.12	50.98	6.60	6.22	6.44	5.99	6.03	6.26
200	1.1	9.63	8.02	7.55	**8.88***	9.00	8.62	57.23	59.68	59.68	64.71	62.58	60.78
	1.5	**12.65***	15.78	14.70	9.46	11.97	12.91	43.19	41.53	41.84	45.97	46.94	43.89
	2	17.44	**23.28***	24.40	25.28	22.25	22.53	32.52	29.31	29.43	28.85	29.72	29.97
	2.5	24.64	**30.62***	34.04	33.28	26.28	29.77	24.07	20.46	21.16	21.43	25.27	22.48
	3	36.38	32.08	35.25	35.68	**34.34***	34.75	20.02	19.38	20.20	19.13	18.47	19.44
	4	37.33	44.99	47.63	40.33	**41.47***	42.35	15.82	14.75	14.30	14.88	14.45	14.84
	6	50.28	51.06	**48.68***	48.99	44.65	48.73	12.82	12.42	12.18	12.49	12.26	12.43
300	1.1	5.16	6.28	5.69	2.93	**4.88***	4.99	86.75	89.84	94.22	91.45	86.05	89.66
	1.5	10.84	12.14	6.78	**7.23***	6.36	8.67	62.36	64.20	66.82	71.50	69.25	66.82
	2	16.00	**18.46***	19.91	19.10	17.65	18.22	45.03	46.22	42.43	46.53	45.52	45.15
	2.5	**24.95***	25.96	23.79	24.98	23.46	24.63	33.26	32.44	33.80	36.24	35.59	34.26
	3	**31.93***	23.64	32.89	27.28	36.88	30.52	28.73	30.86	27.55	28.02	27.03	28.44
	4	**38.79***	36.23	41.51	38.10	42.10	39.35	23.70	21.17	21.83	21.51	21.32	21.91
	6	44.69	48.49	42.70	48.32	**46.63***	46.17	19.26	18.16	18.53	18.30	19.20	18.69
	6	35.98	38.22	41.65	38.54	**38.60***	38.60	37.42	36.83	37.36	37.36	37.48	37.29
400	1.1	3.40	4.02	2.46	**3.48***	4.05	3.48	116.91	124.40	120.96	113.75	108.11	116.83
	1.5	8.24	5.18	6.27	5.85	**6.36***	6.38	84.72	87.80	92.35	89.89	90.42	89.04
	2	14.95	15.60	14.57	**14.36***	12.09	14.31	61.82	58.28	60.11	59.91	62.30	60.48
	2.5	**20.89***	19.96	21.46	14.93	27.72	20.99	44.53	42.59	48.61	46.55	42.60	44.98
	3	24.23	**28.57***	25.50	32.27	25.35	27.18	39.39	19.38	36.45	35.74	34.98	33.19
	4	35.75	37.29	**37.94***	42.07	40.11	38.63	30.57	29.19	28.45	28.42	28.03	28.93
	6	44.89	43.23	40.14	44.07	**43.10***	43.09	25.25	24.66	24.34	25.15	24.61	24.80
600	1.1	1.54	1.08	2.10	2.50	**1.96***	1.83	176.60	185.67	168.38	169.94	167.32	173.58
	1.5	3.95	2.70	**2.77***	4.62	1.84	3.18	126.56	138.32	135.53	129.20	140.85	134.09
	2	12.21	10.67	8.16	10.17	**8.34***	9.91	91.25	88.96	93.24	88.97	89.14	90.31
	2.5	14.83	16.88	**10.63***	10.17	8.34	12.17	65.69	70.03	68.61	71.06	67.93	68.66
	3	19.66	15.90	25.34	27.23	**22.78***	22.18	59.59	55.57	54.03	54.73	58.62	56.51
	4	32.27	31.20	35.97	38.29	**32.74***	34.10	44.87	43.34	54.03	43.24	44.79	46.05

3.4 Quantitative analysis of pre-crack information under the PLD of crack length

The above is a qualitative description of the crack distribution. In order to understand more deeply the influence of the crack distribution on the mechanical properties of the specimen, it is necessary to quantitatively study the crack distribution information under the PLD. Therefore, the distribution information of cracks is statistically analyzed, as shown in Figs. 8-10.

Fig. 8 shows the theoretical and simulated (the called times of DFN is 1) distributions of crack lengths with different PLIes when the NPCs are 50. It should be pointed out that the abscissa of Fig. 8 indicates the serial number of 50 cracks arranged from long to short size. The theoretical distribution curve is determined by Eqs. (1)-(3), and the simulated distribution is obtained by FISH language compilation and extraction. It can be seen that the theoretical distribution is basically consistent with the simulated distribution, and when the PLI is small, the decreasing rate of crack length changes continuously and smoothly (such as the crack distribution corresponding to b=1.1). As the PLI increases, the two phases of faster and slower for decrease of the crack length gradually become more obvious, and when b=6, the crack length rapidly reduces from 10 to 1 and then remained nearly unchanged.

The relationship between the total length l_p, the NPC and the PLI also can be obtained by the compilation and extraction of FISH language, as shown in Fig. 9. It can be seen from Fig. 9(a) that under different PLIes, the total length of the pre-crack increases linearly with the total crack number, and the smaller the PLI, the larger the increase rate of the total crack length. As can be seen from Fig. 8, this is because the larger the PLI is, the closer the crack length is to the minimum crack length set. For the specimens with same pre-crack number, the total length of the pre-cracks decreases with a decreasing rate as the PLI, and the larger the NPC, the more obvious the total length of the pre-cracks decreases.

4. Simulation results

4.1 Variation characteristics of sandstone strength based on NPC and PLI

The UCS and the total length of the pre-cracks contained in the 210 models are obtained by the FISH program and shown in Table 3. And the quantitative relationships between UCS (or its mean value) and pre-crack information of sandstone can be obtained by the information extraction and processing from Table 3, as can be seen from Figs. 11-13.

Fig. 10 shows the relationship between UCS and the total pre-crack length of 210 specimens in Table 3. It can be seen that the rock UCS decreases with a decreasing rate as the increase of the total pre-crack length. Specifically, when the total pre-crack length increases from 0 to 0.5 m, the UCS reduces from about 50 MPa to 20 MPa, the reduction exceeds 30 MPa (which is based on the trend line obtained by fitting, see Fig. 11), and when the pre-crack length

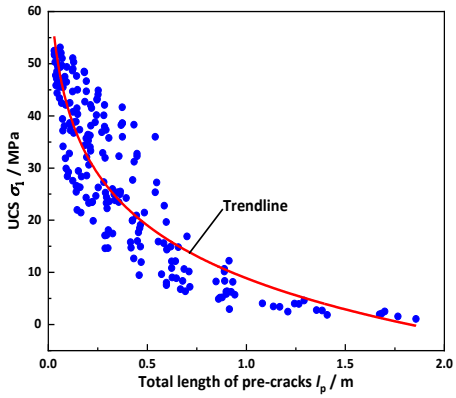

Fig. 10 Correspondence between the UCS and total length of pre-cracks for 210 specimens in Table 3

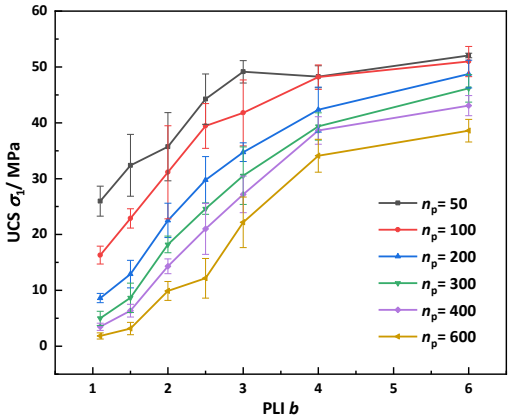

(a) Variation of UCS with the PLI

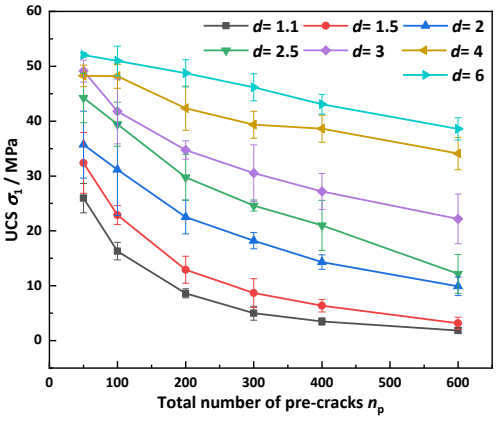

(b) Variation of UCS with the NPC

Fig. 11 Relationship between UCS, PLI and the NPC of sandstone

increases from 0.5 m to 1.8 m, the UCS only slightly reduces by 18 MPa (from 20 MPa to about 2 MPa, see Fig. 11).

Fig. 11 shows relationship between UCS, PLI and the NPC of sandstone. When the NPC is constant, the rock UCS shows a decelerated growth trend with the PLI (see Fig. 11(a)). And the fewer the NPC under the same PLI, the greater the UCS value of sandstone. It can be seen from Fig. 11(b) that as the NPC increases, the rock strength decreases as a whole. And with the increase of the PLI, the UCS reduction process of sandstone changes the form from

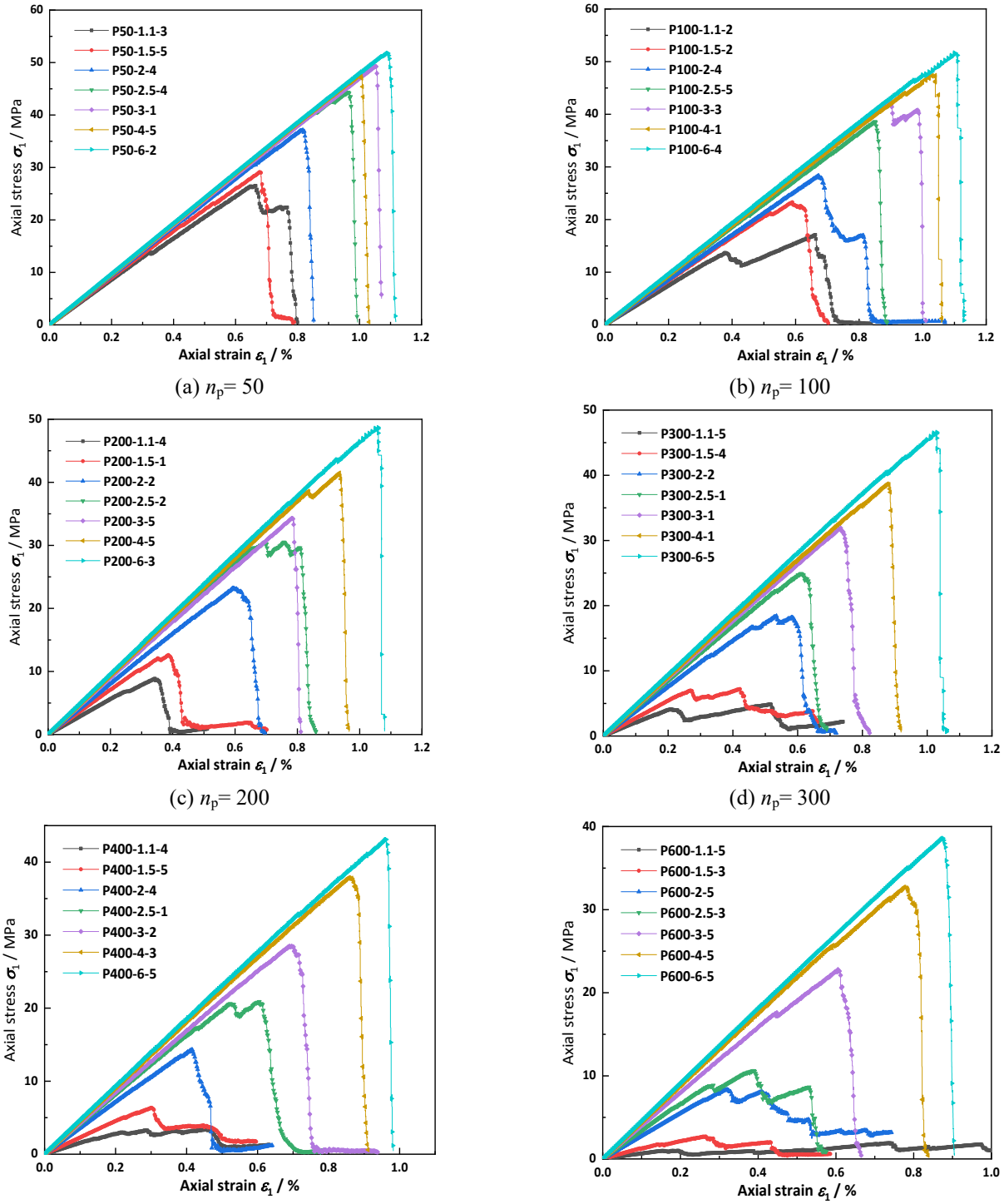

Fig. 12 Full stress-strain curve of representative specimens in each big groups

an inverse function to a linear function. The reason for the above variations is that the UCS of sandstone decreases with the increase of the pre-crack length (see Fig. 10), and the increase of the PLI and the NPC respectively leads to the decrease and increase of the pre-crack length when other conditions are the same (see Fig. 9).

4.2 Stress-strain curves of representative specimens

Since the amount of data in Table 3 is too large, so the specimens whose UCSs (marked with * and bolded, see Table 3) are closest to the mean value of each group and their other mechanical properties are mainly selected as the representative to display in this section and the following text.

The full stress-strain curves of representative specimens in each group are shown in Fig. 12. It can be seen that when the NPC is the same, both the rock strength and elastic modulus show an increasing trend with the PLI. And with the increase of the PLI, the post-peak curve of the specimen

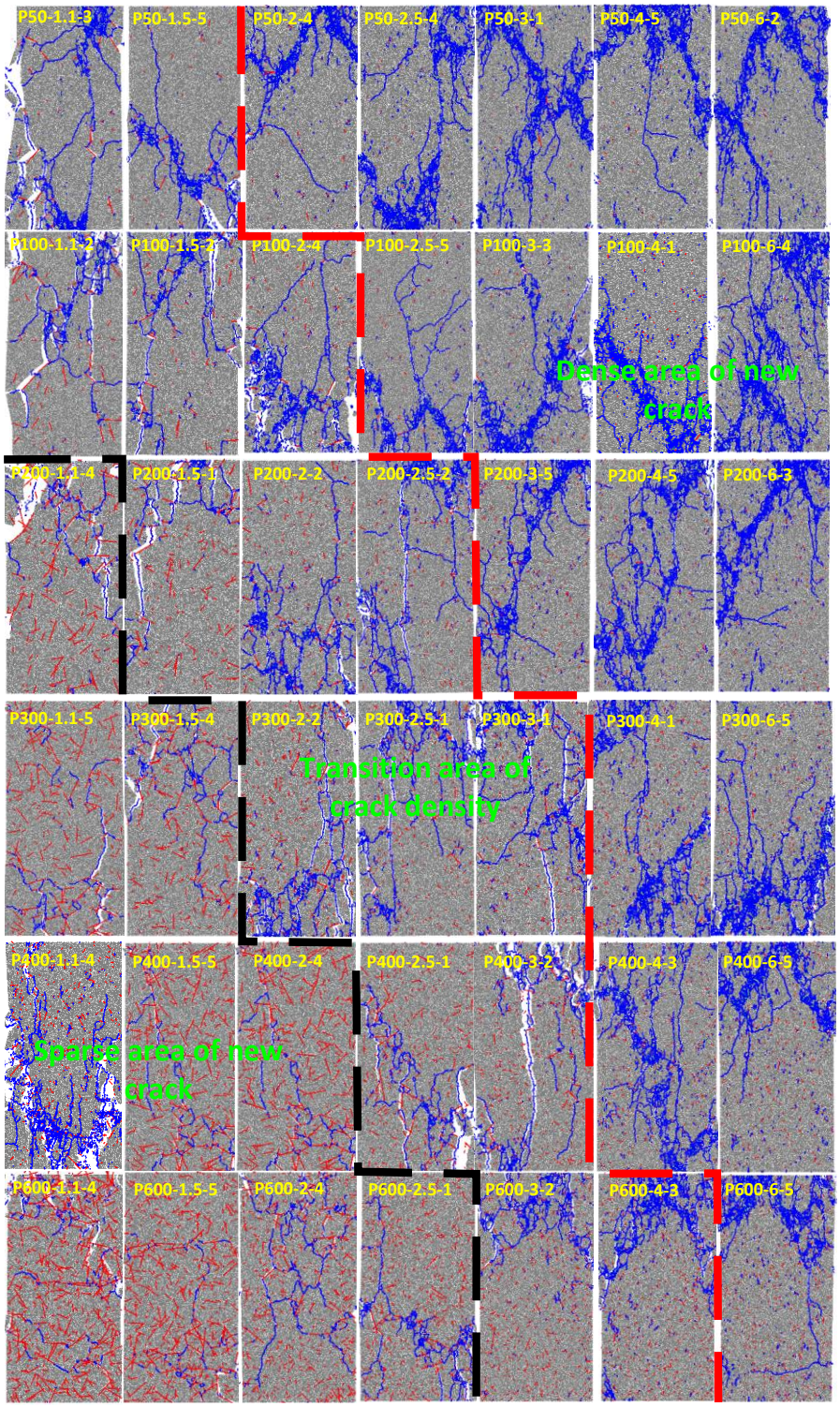

Fig. 13 Failure modes of sandstone specimens corresponding to the stress-strain curves in Fig. 12 (Red, blue, and green lines respectively represent pre-cracks, tensile cracks and shear cracks (very few))

changes from a relatively slow decline to a sharp drop, which indicates that the characteristic of brittle failure for defected specimen increases with the PLI.

In addition, with the increase of the NPC, the strength difference of the specimens under the adjacent PLI distribution increases as a whole, and both the absolute and relative values of the specimen strength differences under the PLI of 1.1 and 6 show the increasing trend. For example, for the specimen with the NPC of 50, the difference between the maximum and minimum values of UCS is 25.33 MPa, while which of the specimens with the NPC of 600 is 36.64 MPa.

4.3 Failure mode of representative specimens

The final failure modes of the sandstone corresponding

to the stress-strain curves in Fig. 12 are shown in Fig. 13. Under the condition of uniaxial loading, the tensile crack rather than the shear crack is the main form of micro-failure between particles inside the specimens.

When the NPC is the same, the number of newly generated cracks increases with the PLI; while when the PLI is the same, the number of new cracks generated corresponding to rock failure decreases with the NPC. In summary, when the NPCs is large and the PLI is small, the new cracks generated corresponding to rock failure are less, as shown in the lower left corner of Fig. 13. When the NPC is small and the PLI is large, more new cracks are generated, as can be seen in the upper right corner of the Fig. 13.

Based on which, Fig. 12 can be roughly divided into three parts according to the number of new cracks, namely the crack sparse area, the crack dense area and the crack density transition area therebetween (see Fig. 13). With calculation (see Table 3), the total length ranges of the pre-cracks in the three parts (sparse area, transition area and dense area) are less than 0.2 m, between 0.2- 0.55 m and greater than 0.55 m.

As shown in Fig. 13, the failure intensity of the specimen gradually becomes weaker as the total length of the pre-crack increases, which is closely related to the damage energy of the specimen (Wu *et al.* 2018a). For the specimens in crack dense area, their failures are mainly the penetration of pre-cracks with lower rock strength (see Fig.12 and Fig.13), but for the specimens in crack sparse area, both their strength and failure energy are very large, the distinct rupture zones are formed by accumulated cracks during the process of the specimen failure (see Fig.13). What's more, for the specimens in the crack density transition area, there are obvious gaps between the rock blocks, which indicates that significant lateral expansion occurred during the failure of the specimen under the combined action of proper crack cutting and failure energy (Qin *et al.* 2019, Zhang *et al.* 2015).

5. Discussion

5.1 Rock strength evolution based on PLD of pre-crack length

According to the PLD form of the crack length corresponding to Eq. (1) and assuming that the specific crack length is approximately obtained by the linear difference, the adjacent three difference points can be set as (x_1, y_1), $(x_1+\Delta x, y_2)$ and $(x_1+2\Delta x, y_3)$.

Therefore, the following formulas can be obtained,

$$f_{21}=\frac{y_2}{y_1}=\frac{a(x_1+\Delta x)^{-\frac{1}{b-1}}}{ax_1^{-\frac{1}{b-1}}} \tag{4}$$

$$f_{32}=\frac{y_3}{y_2}=\frac{a(x_1+2\Delta x)^{-\frac{1}{b-1}}}{a(x_1+\Delta x)^{-\frac{1}{b-1}}} \tag{5}$$

Eq. (6) can be obtained by dividing Eq. (5) and Eq. (4),

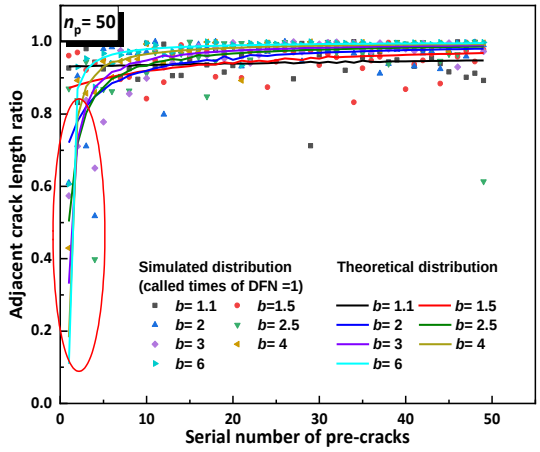

Fig. 14 Ratios of adjacent crack lengths for simulation and theoretical distribution

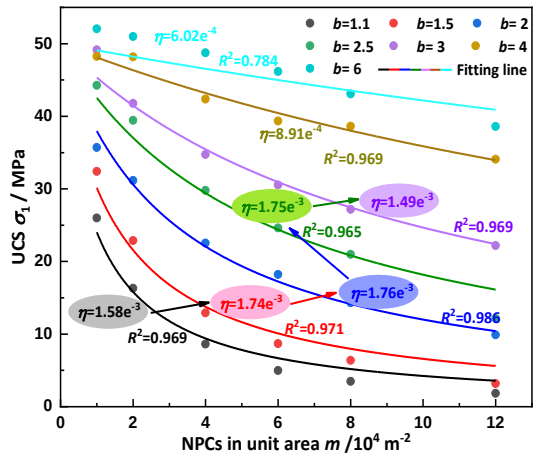

Fig. 15 Comparison of the theoretical and the simulation results for sandstone strength

$$\frac{f_{32}}{f_{21}}=\left(\frac{x_1^2+2x_1\Delta x}{x_1^2+2x_1\Delta x+\Delta x^2}\right)^{-\frac{1}{b-1}} \tag{6}$$

When $\Delta x \ll x_1$, the quadratic term Δx^2 can be negligible. So Eq. (6) can be simplified as follows,

$$\frac{f_{32}}{f_{21}}\approx 1 \tag{7}$$

Eq. (7) shows that the crack length, arranged in order of size, is approximately a geometric progression.

Ratios of adjacent crack lengths for simulation and theoretical distribution are shown in Fig. 14. It can be seen that the theoretical and simulation results are basically consistent with each other and concentrated between 0.9 and 1.0. However, it is observed that when the PLI is large, the theoretical and simulation results near the longest pre-crack in Fig. 14 are extremely small (as shown in the red ellipse, see Fig. 14). Which is because that when the index is large, the crack size near the longest crack varies greatly and its number is extremely small (see Fig. 8). It is also because of which (see Fig. 8 and Fig. 14), the crack lengths arranged from large to small can be approximately seen as

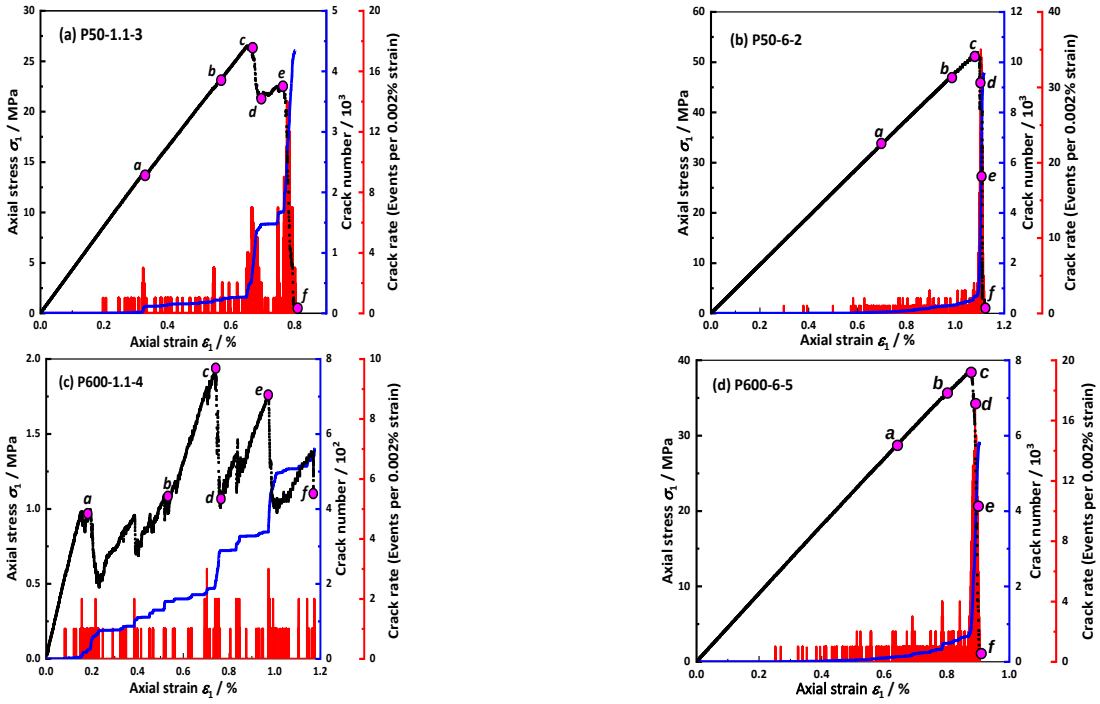

Fig. 16 Evolution curves of stress and crack for the four representative specimens in Fig. 13

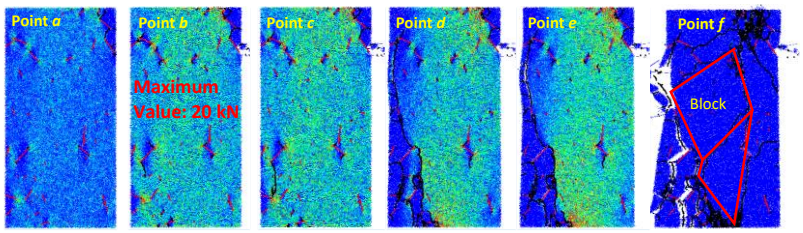

(a) Specimen P50-1.1-3

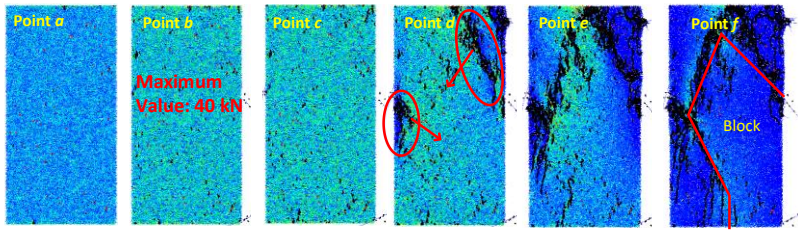

(b) Specimen P50-6-2

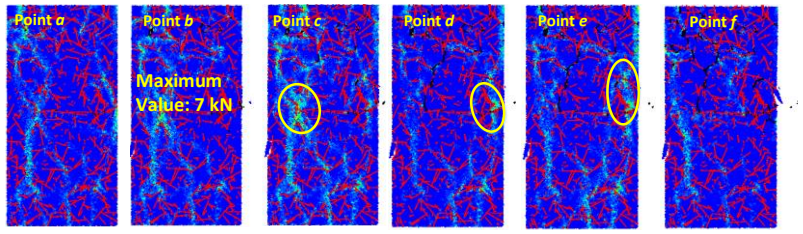

(c) Specimen P600-1.1-2

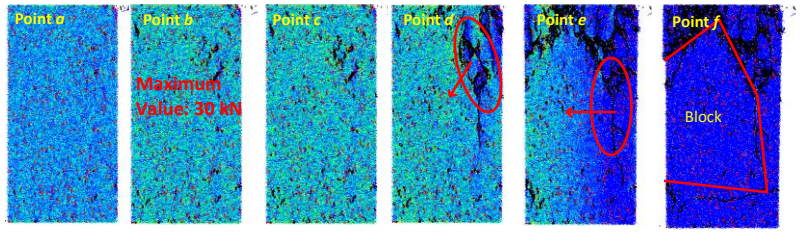

(d) Specimen P600-6-5

Fig. 17 Force field evolution during loading process for typical specimens

geometric progression.

Therefore, according to the longest crack length l_{max} set in Section 2, the total length of n pre-cracks inside specimen can be obtained by the Eq. (8),

$$l_{\max}+kl_{\max}+k^2l_{\max}+\mathrm{L}+k^{n-1}l_{\max}=\frac{k^n-1}{k-1}l_{\max} \tag{8}$$

where k can be determined according to the following formula,

$$k^{n-1}l_{\max}=l_{\min} \tag{9}$$

From Eqs. (8) and (9), the average half length of the pre-cracks inside the specimen can be determined as follows,

$$d=\frac{k^n-1}{2n(k-1)}l_{\max} \tag{10}$$

For the two-dimensional plane with distributed cracks, the effective elastic modulus $\tilde{E}$ of the material can be obtained by the Mori-Tanaka method (M-T) as follows (Benveniste 1986),

$$\begin{cases}\tilde{E}=\dfrac{E_i}{1+\pi\alpha}\\ \alpha=md^2\end{cases} \tag{11}$$

where α, E_i denote the pre-crack density parameter and the elastic modulus of the intact specimen, respectively; $m=\dfrac{n}{S}$ is the crack number per unit area and S denotes for the area of the specimen.

The rock damage defined by the elastic modulus method can be described as follows (Mukhopadhyay and Hallett 2019, Shi *et al.* 2019),

$$D=1-\frac{\tilde{E}}{E_i} \tag{12}$$

The relationship between effective stress $\overset{\circ}{\sigma}$ and damage D can be expressed as,

$$\tilde{\sigma}=\frac{\sigma_1}{1-D} \tag{13}$$

According to Eqs. (11)-(13), the correlation between $\tilde{\sigma}$ and m, d can be obtained as follows,

$$\tilde{\sigma}=\sigma_1(1+\pi md^2) \tag{14}$$

The UCS of the non-destructive specimen (see Fig. 4) is used as the maximum allowable stress σ_a (the maximum effective stress), so that the strength σ_1 of the damage specimen is as follows,

$$\sigma_1=\frac{\sigma_a}{1+\pi md^2} \tag{15}$$

Due to the fact that the Eq. (11), reacted to the superposition of the material weakening effect caused by all pre-cracks inside the specimen, is more suitable for specimen with less number and uniform-distributed pre-cracks (included the crack length). However, when the NPC is too large inside the specimen, the random arrangement of the pre-cracks will be overlapped to form the new long pre-cracks. Based on which, the crack density factor η is introduced to correct the crack density parameter α. At this point, the damage model of rock strength was established as follows,

$$\sigma_1=\frac{\sigma_a}{1+\eta\pi md^2} \tag{16}$$

The comparison of the fitting curves (obtained by Eq. (16)) and the simulation result is shown in Fig. 15, it can be seen that the fitting and simulation results are almost completely coincident with each other. By which the rationality of damage strength model in this article can be verified. What's more, when the PLI of the crack length is not more than 4, the crack density factors η is equal to about 1.7×10^{-3}, and when the PLI is greater than or equal to 4, the crack density factors is significantly reduced. Which is because that when the PLI is greater than 4, the crack length distribution is significantly different from the standard geometric progression (see the red ellipse in Fig. 14), so the average half length of the pre-cracks calculated according to Eqs. (8)-(10) is larger than the simulation results.

5.2 Evolution of force field in specimen failure process

According to Figs. 12 and 13, the rock strength and the characteristics of the failure mode are continuously changing as the NPC and the PLI of the crack length (see Section 4.1). Therefore, based on the layout considerations, only the specimens of the four corners in Fig. 13 are selected as the representative for the analysis of the force field evolution. The four specimens respectively represent the crack information of the minimum PLI and NPC (specimen P50-1.1-3), the minimum PLI and maximum NPC (specimen P50-6-2), the maximum PLI and minimum NPC (specimen P600-1.1-4) and the maximum PLI and NPC (specimen P600-6-5).

The stress and crack evolution curves of the representative specimens during the loading failure process are shown in Fig. 16. It can be seen that when the PLI is 1.1, the stress curve is more volatility, and which is increased with the NPC. When the NPC reaches 600, the stress curve fluctuates significantly even before the peak stress. While for the specimens with the PLI of 6, whose axial stress falls sharply after just reaches the peak stress, show obvious brittle failure characteristics.

It can be seen from the crack propagation curves that for sandstone specimens with the PLI of 1.1, the cracks in the pre-peak stage have been generated in large quantities. And for the specimens with the NPC of 600, the number of crack generated has even reached half of the total crack number (Zhao *et al.* 2015). But for the specimen with the PLI of 6, the amount of new cracks before the peak stress is extremely small, accounting for only about one-tenth to one-sixth of the total crack number. According to the crack rate curve (characterized by the crack number per unit strain), when the NPC is the same, with the increase of PLI,

the evolution of the specimen crack events for the changes from multi-peak and low extremum (see Fig. 16(c)) to single peak and high extremum (see Fig. 16(d)).

In Fig. 16, the number of cracks corresponding to point *a* is about one tenth of the total crack number at the peak stress (point c), which is taken as the crack initiation stress (Ghazvinian and Diederichs 2018, Wu *et al.* 2018b, Yang 2014). Therefore, points *a*, *c*, and *f* in Fig. 16 indicate the crack initiation stress, the peak stress, and the final failure stress respectively.

The point *b* is the stress point between points *a* and *c*, while the points *d* and *e* are selected between the stress points *c* and *f*. By extracting the variation of the internal force field of the specimens corresponding to the above 6 points, the influence of NPC and PLI on the failure mechanism of sandstone is analyzed.

The UCS of each specimen has a large difference, in order to better describe the change of the stress field, the maximum values of the force fields of each specimen in Fig. 17 are set as 20 kN, 40 kN, 7 kN and 30 kN, respectively. For the specimen P50-1.1-3 and P600-1.1-2, there is a strong cutting effect on the specimens due to the large scale of the pre-cracks, which results in the force being easily concentrated in the rock bridge, as shown by the yellow ellipses corresponding to Fig. 17(a)and Fig. 17(c).

For the specimens P50-6-2 and P600-6-5, the scale of pre-cracks is extremely small because of the large PLI (see Fig. 17(b)and Fig. 17(d)), which results in the uniform crack distribution and small crack cutting effect. So the two specimens can be regarded as the intact samples with the lower strength parameters, which is the main reason for the even distributed force field before the specimen is loaded to the peak stress.

When loaded into the post-peak stage, all the specimens are basically gradually destroyed from the boundary to the middle part (see the red ellipses and arrows in Fig. 17). For the specimens P50-1.1-3 and P600-1.1-2, the number of newly generated cracks is small. while for the specimen P600-6-5, whose UCS is relatively high and the damage process is more severe (see Fig. 17). For the specimen P600-1.1-2, because the number and the scale of the cracks contained are larger, the failure process of the specimen is only the interpenetration of the pre-cracks, so the change of the stress field in the process is relative small (see Fig. 17).

In addition, as mentioned in Section 4.3, the rock blocks corresponding to final failure of specimens in the crack-dense area are large due to the small pre-crack size (see Figs. 17(b)and (d)), and the specimen in the crack sparse area is very broken caused by the cutting effect of larger size cracks (see Fig. 17(c)). Therefore, no significant block separation occurred in the specimens in the two regions (see Figs. 17(b)and (d)).

6. Conclusions

In this paper, the PLI and the NPC are changed to statistically study the effects of pre-crack on the mechanical properties of sandstone and meticulously analyze the corresponding failure process, and then the damage model of specimen with pre-crack length following PLD is established. The main conclusions are as follows,

- With the increase of the PLI, the proportion of prefabricated long cracks gradually decreases.
- The UCS of sandstone decreases as the total length of the pre-cracks. Specifically, when the NPC is the same, the UCS of sandstone increases with the PLI; while when the PLI is the same, the UCS decreases with the NPC.
- The damage model of rock strength is established based on the M-T method, and the theoretical formula can better describe the strength evolution of damaged rock. That is, as the PLI increases, the relationship between the rock UCS and the crack number per unit area *m* changes the form from an inverse function to a linear function.
- The failure mode of the specimen is closely related to the total length of the pre-cracks. For the specimens with total pre-crack length less than 0.2 m, their obvious brittle failure is accompanied by a large number of cracks; For the specimens with total pre-crack length greater than 0.55 m, their failure process is main the interpenetration of the pre-cracks with little new cracks generated; For the specimens with the pre-crack length between 0.2-0.55 m, significant lateral expansion occurred during their failure process.
- For the specimens with smaller PLI, the concentration of the force field inside is very serious in the pre-peak loading process; while for the specimen with larger PLI, which is relative uniform.

Acknowledgments

Financial supports for this work, the Fundamental Research Funds for the Central Universities (No. 2018ZDPY08) and National Natural Science Foundation of China (No. 41974164), are gratefully acknowledged.

References

Afolagboye, L.O., He, J. and Wang, S. (2017), "Experimental study on cracking behaviour of moulded gypsum containing two non-parallel overlapping flaws under uniaxial compression", *Acta. Mech. Sinica Prc.*, **33**(2), 394-405. https://doi.org/10.1007/s10409-016-0624-9.

Al-Aasm, I.S., Mrad, C. and Packard, J. (2019), "Fluid compartmentalization of Devonian and Mississippian dolostones, Western Canada Sedimentary Basin: petrologic and geochemical evidence from fracture mineralization", *Can. J. Earth Sci.*, **56**(3), 265-305. https://doi.org/10.1139/cjes-2018-0226.

Basson, I.J. and Viola, G. (2003), "Structural overview of selected Group II kimberlite dyke arrays in South Africa: implications for kimberlite emplacement mechanisms", *S. Afr. J. Geol.*, **106**(4), 375-394. https://doi.org/10.2113/106.4.375.

Benveniste, Y. (1986), "On the Mori-Tanaka's method in cracked bodies", *Mech. Res. Commun.*, **13**(4), 193-201. https://doi.org/10.1016/0093-6413(86)90018-2.

Castro-Filgueira, U., Alejano, L.R., Arzúa, J. and Ivars, D.M. (2017), "Sensitivity analysis of the micro-parameters used in a PFC analysis towards the mechanical properties of rocks", *Proc. Eng.*, **191**, 488-495.

https://doi.org/10.1016/j.proeng.2017.05.208.

Chen, G.W., Song, L. and Zhang, R.R. (2018), "Modeling acoustic attenuation of discrete stochastic fractured media", *Acta. Geod. Geophys.*, **53**(4), 679-690. https://doi.org/10.1007/s40328-018-0237-9.

Ghazvinian, E. and Diederichs, M.S. (2018), "Progress of brittle microfracturing in crystalline rocks under cyclic loading conditions", *J. S. Afr. I. Min. Metall.*, **118**(3), 217-226. https://doi.org/10.17159/2411-9717/2018/v118n3a4.

Huang, Y.H., Yang, S.Q. and Zhao, J. (2016), "Three-dimensional numerical simulation on triaxial failure mechanical behavior of rock-like specimen containing two unparallel fissures", *Rock Mech. Rock Eng.*, **49**, 1-19. https://doi.org/10.1007/s00603-016-1081-2.

Lei, Q.H. and Gao, K. (2019), "A numerical study of stress variability in heterogeneous fractured rocks", *Int. J. Rock Mech. Min. Sci.*, **113**, 121-133. https://doi.org/10.1016/j.ijrmms.2018.12.001.

Lenton, A., McInnes, K.L. and O'Grady, J.G. (2015), "Marine projections of warming and ocean acidification in the Australasian region", *Aust. Meteorol. Ocean.*, **65**(1), 1-28. https://doi.org/10.22499/2.6501.012.

Mukhopadhyay, S. and Hallett, S.R. (2019), "A directed continuum damage mechanics method for modelling composite matrix cracks", *Compos. Sci. Technol.*, **176**, 1-8. https://doi.org/10.1016/j.compscitech.2019.03.022.

Qin, Z., Fu, H. and Chen, X. (2019), "A study on altered granite meso-damage mechanisms due to water invasion-water loss cycles", *Environ. Earth Sci.*, **78**(14), 428. https://doi.org/10.1007/s12665-019-8426-6.

Shan, P.F. and Lai, X.P. (2019) "Mesoscopic structure PFC similar to 2D model of soil rock mixture based on digital image", *J. Vis. Commun. Image R.*, **58**, 407-415. https://doi.org/10.1016/j.jvcir.2018.12.015.

Shi, H., Zhang, H.Q., Song, L. and Wu, Y. (2019), "Variation of strata pressure and axial bolt load at a coal mine face under the effect of a fault", *Arch. Min. Sci.*, **64**(2), 351-374. https://doi.org/10.24425/ams.2019.128688.

Storey, B.C., Vaughan, A.P.M. and Riley, T.R. (2013), "The links between large igneous provinces, continental break-up and environmental change: evidence reviewed from Antarctica", *Earth Environ. Sci. Trans. R. Soc.*, **104**(1), 17-30. https://doi.org/17-30. 10.1017/S175569101300011X.

Wang, J., Li, S.C, Li, L.P., Lin, P., Xu, Z.H. and Gao, C.L. (2019), "Attribute recognition model for risk assessment of water inrush", *Bull. Eng. Geol. Environ.*, **78**(2), 1057-107. https://doi.org/10.1007/s10064-017-1159-4.

Wang, P.T., Ren, F.H. and Cai, M.F. (2018), "Mechanical analysis and size effect of rough discrete fractures network model under direct shear tests based on particle flow code", *J. China Coal Soc.*, **43**(4), 976-983. https://doi.org/10.13225/j.cnki.jccs.2017.1061. (in Chinese).

Wang, X. and Tian, L.G. (2018), "Mechanical and crack evolution characteristics of coal–rock under different fracture-hole conditions: a numerical study based on particle flow code", *Environ. Earth Sci.*, **77**(8), 297. https://doi.org/10.1007/s12665-018-7486-3.

Wu, J.Y., Feng, M.M., Mao, X.B., Xu, J.M., Zhang, W.L., Ni, X.Y. and Han, G.S. (2018a), "Particle size distribution of aggregate effects on mechanical and structural properties of cemented rockfill: Experiments and modeling", *Constr. Build. Mater.*, **193**, 295-311. https://doi.org/10.1016/j.conbuildmat.2018.10.208.

Wu, J.Y., Feng, M.M., Yu, B.Y. and Han, G.S. (2018b), "The length of pre-existing fissures effects on the mechanical properties of cracked red sandstone and strength design in engineering", *Ultrasonics*, **82**(1), 188-199. https://doi.org/10.1016/j.ultras.2017.08.010.

Yang, S.Q., Huang, Y.H., Jing, H.W. and Liu, X.R. (2014), "Discrete element modeling on fracture coalescence behavior of red sandstone containing two unparallel fissures under uniaxial compression", *Eng. Geol.*, **178**, 28-48. https://doi.org/10.1016/j.enggeo.2014.06.005.

Yang, Z.M., Gao Y.T., Wu, S.C., Cheng, Z.Q. and Jin, A.B. (2018), "Study of the influence of joint parameters on rock mass strength based on equivalent rock mass technology", *J. China Univ. Min/ Technol.*, **47**(5), 979-986. https://doi.org/1000-1964 (2018)05-0979-08 (in Chinese).

Zhang, H.Q., Tannant, D.D., Jing, H.W., Nunoo, S., Niu, S.J. and Wang, S.Y. (2015), "Evolution of cohesion and friction angle during microfracture accumulation in rock", *Nat. Hazards*, **77**(1), 497-510. https://doi.org/10.1007/s11069-015-1592-2.

Zhang, X.P. and Zhang, Q. (2017), "Distinction of crack nature in brittle rock-like materials: A numerical study based on moment tensors", *Rock Mech. Rock Eng.*, **50**(10), 1-9. https://doi.org/10.1007/s00603-017-1263-6.

Zhao, W.H., Huang, R.Q. and Yan, M. (2015) "Study on the deformation and failure modes of rock mass containing concentrated parallel joints with different spacing and number based on smooth joint model in PFC", *Arab. J. Geosci.*, **8**, 7887-7897. https://doi.org/10.1007/s12517-015-1801-z.

Zhu, J.Q. and Yang, X.L. (2018), "Probabilistic stability analysis of rock slopes with cracks", *Geomech. Eng.*, **16**(6), 655-667. https://doi.org/10.12989/gae.2018.16.6.655.

CC